journal

J. Am. Ceram. Soc., 89 [3] 1028–1036 (2006)
DOI: 10.1111/j.1551-2916.2005.00788.x


# Phases in Ceria–Zirconia Binary Oxide $(1-x)CeO_2$–$xZrO_2$ Nanoparticles: The Effect of Particle Size

Feng Zhang and Chih-Hao Chen

Department of Applied Physics and Applied Mathematics, Materials Research Science and Engineering Center, Columbia University, New York, New York 10027

Jonathan C. Hanson

Department of Chemistry, Brookhaven National Laboratory, Upton, New York 11973

Richard D. Robinson, Irving P. Herman, and Siu-Wai Chan*,†

Department of Applied Physics and Applied Mathematics, Materials Research Science and Engineering Center, Columbia University, New York, New York 10027

**The phases of ceria–zirconia nanoparticles observed in air are studied as a function of particle size and composition by X-ray diffraction, transmission electron microscopy, and Raman spectroscopy. The emergence of two tetragonal phases $t''$ and $t$ monotonically moves toward higher zirconia concentrations with decreasing particle size. A smaller particle size increases the solubility of zirconia in cubic ceria, while higher zirconia content in ceria stabilizes against coarsening. In particular, the cubic $Ce_{1-x}Zr_xO_{2-y}$ is persistent and is 8% in phase amount even at 90% zirconia with 33 nm crystal size. Neither the monoclinic phase $m$ nor the tetragonal phase $t'$ is observed in the present nanoparticles (<40 nm). The effectiveness of these nanoparticles as oxygen source-and-sink in catalytic support is largely due to the persistence of the cubic and the $t''$ phases.**

## I. Introduction

Cerium oxide, in cubic fluorite structure, has been widely investigated as a key component in three-way catalysts,[1] as an electrolyte for solid oxide fuel cells,[2] and as a catalyst for the water–gas shift reaction.[3] Under a reducing environment, cerium dioxide (i.e., $CeO_2$) releases oxygen to become reduced ceria (i.e., $CeO_{2-y}$), while in ambient and oxidizing conditions this reduced ceria can absorb oxygen and change back to $CeO_2$.[1] This reversible behavior is possible as long as ceria maintains its cubic fluorite structure through the reduction–oxidation (redox) processes. This property, which is the alleged source of the oxygen storage capacity (OSC) of ceria, is much enhanced by a large surface area and a small particle size. Particle-size stability at high temperatures is a major issue for pure ceria, however. At high temperatures, ceria particles are easily coarsened, resulting in a smaller total surface area and a lower catalytic efficiency. Ceria mixed with different metal oxides has been studied to resolve this issue.[4–7] However, the addition of other metal oxides can render the instability of the ceria fluorite phase which is the basis of the OSC property. The binary oxide system of ceria and zirconia has drawn much attention because of its superb redox properties and thermal stability against coarsening.[5]

To optimize the catalytic properties, it is important to understand the structure of the $CeO_2$–$ZrO_2$ binary oxide system. An early phase diagram of the binary oxide $CeO_2$–$ZrO_2$ was established in 1950[8] (see Fig. 1), while later on, a more in-depth phase diagram was published by Yashima[9] (see Fig. 2). From these diagrams, the phase amount of the cubic fluorite phase at 35%–40% zirconia is at most 50%, but this composition is used for many OSC applications. The perplexing issue is why would a 50% phase amount be an optimum solution as the cubic fluorite phase is the active OSC element.

As reported, there are five phases that exist in the $CeO_2$–$ZrO_2$ binary system from room temperature to 900°C. At a $ZrO_2$ concentration higher than 95%, the equilibrium is 100% monoclinic phase with a space group of $P2_1/c$. At the other composition end, corresponding to a high ceria concentration ($Ce_{1-x}Zr_xO_{2-y}$ with $x<15\%$), the stable phase is the cubic fluorite structure ($Fm3m$), which is the important phase for catalysis as its oxygen ions are mobile and oxygen deficiency is accom-

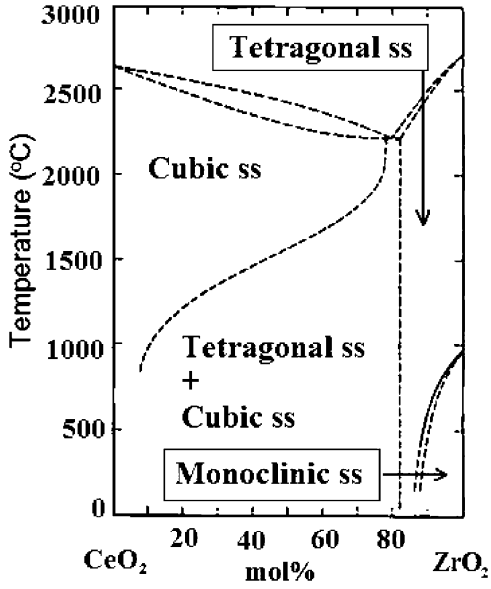


**Fig. 1.** Phase diagram of $CeO_2$–$ZrO_2$ from Duwez and Odell.[8] The cubic solid solution occurs below 10% $ZrO_2$-doped $CeO_2$ below 900°C.

T. M. Gur—contributing editor

Manuscript No. 20907. Received September 27, 2004; approved September 23, 2005.
Paper was presented as an invited talk at the 106th Annual Meeting of the American Ceramic Society, April 20, 2004, Indianapolis, IN. This work is primarily supported by the National Science Foundation MRSEC Program under DMR-0213574 and partly by NYSTAR DOE DE-FG02-05 ER15730. Research at the NSLS, BNL is supported by the U.S. Department of Energy, Division of Materials Sciences and Chemical Sciences, under DE-AC02-98CH10886.
*Member, American Ceramic Society.
†Author to whom correspondence should be addressed. e-mail: sc174@columbia.edu

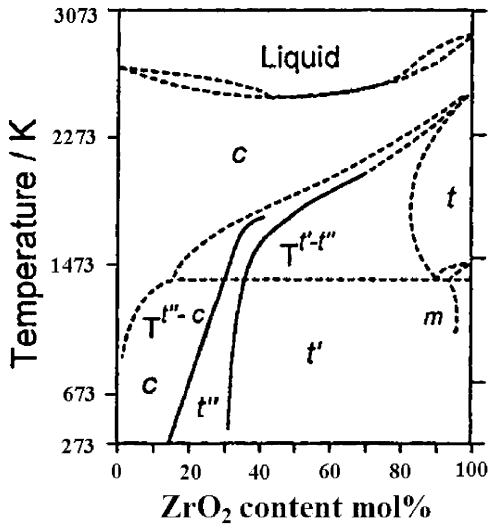


**Fig. 2.** Phase diagram of $CeO_2$–$ZrO_2$ based on Raman and XRD measurements.[9] Only two tetragonal phases, $t'$ and $t''$ (and not t), were observed.

modated by oxygen vacancies. In the intermediate region (i.e., $15\% < x < 90\%$), there are two tetragonal phases, $t'$ and $t''$, that are structurally different from each other. At temperatures higher than 1200°C, the monoclinic phase is unstable and will change to the tetragonal phase $t$. The $t$ phase has a lattice parameter ratio ($c/a$) of 1.4; the $t'$ phase has a $c/a$ ratio of 1.01; and the $t''$ phase has a $c/a$ ratio of 1. As the $t''$ phase and the cubic phase $c$ give identical X-ray diffraction (XRD) patterns, the $t''$ phase is often grouped with the cubic phase $c$ and they are known together as the extended cubic phase $c'$. The cations in the $t''$ phase have the same positions as those in the cubic $c$ phase, but some oxygen ions are displaced from their positions in cubic fluorite. As XRD is not sensitive to light elements (i.e., oxygen) in the presence of heavy elements (i.e., cerium), it is nearly impossible to separate the $t''$ phase from the cubic phase $c$ by XRD alone. Raman scattering from lattice vibrations is sensitive to this tetragonal distortion of the oxygen positions, and is employed in helping to distinguish between the $c$ and $t''$ phases.[9] The $t$ and $t'$ phases can be differentiated from each other by XRD. In the case of the $t'$ phase, the (400) and (004) peaks of its XRD pattern are separate,[9] even though its $c/a$ ratio is close to 1, and therefore it is readily distinguished from the $c'$ phase. For the cubic phase ($c$) of pure ceria, one Raman mode is observed at 464 $cm^{-1}$. For the tetragonal phases $t$, $t'$, and $t''$, which all have space group $P4_2/nmc$, six Raman modes near 131, 247, 307, 464, 596, and 626 $cm^{-1}$, are allowed.[9]

Extensive studies have been conducted on the structural properties of $CeO_2$–$ZrO_2$ bulk binary system.[9] $CeO_2$–$ZrO_2$ nanoparticles prepared from high-energy milling displayed very different phase stability[10] compared with bulk phase diagram.[9] Unfortunately, phases present were not thoroughly discussed.[10] Besides, the large distribution of particle size prohibited any attempt to relate phase stability with particle size. Here, we investigate the structural properties of the $CeO_2$–$ZrO_2$ nanoparticles to provide phase information and particularly to address the following two questions. First, are there methods that can stabilize the $c'$ phase for a higher zirconia concentration to lessen particle coarsening? Second, to what extent does the particle size affect phase stability (which itself has a significant impact on catalysis)?

## II. Experimental Procedure

Precursors of zirconia-ceria binary oxide were prepared by mixing $ZrOCl_2 \cdot 8H_2O$ (Alfa Aesar, Ward Hill, MA, 99.9%) and $Ce(NO_3)_3 \cdot 6H_2O$ (Alfa Aesar, 99.99%) aqueous solutions with hexamethylenetetramine ($(CH_2)_6N_4$, HMT, Lancaster, U.K., 99+%) solutions at room temperature. After centrifugation, the precipitates were dried under ambient conditions, and then annealed in air at temperatures from 600° to 1200°C. The precipitates contained ceria nanocrystals, each surrounded by amorphous zirconia.

The cubic lattice parameter of ceria was observed by *in situ* XRD to contract as the mixing among Ce and Zr ions proceeded and the process was observed to be complete at 750°C. The ramping rate was 100°C/h and the time at the highest temperature was 30 min.[11–13] Therefore, samples annealed at and above 800°C are fully homogenized. The concentrations of cerium and zirconium in the final samples were determined by inductively coupled plasma analysis (ICP).

Synchrotron X-ray radiation, having orders of magnitude higher intensity than standard X-ray sources, provides high-quality XRD patterns with a high signal/noise ratio. This is especially helpful to study complex systems such as the present $CeO_2$–$ZrO_2$ binary oxide. XRD was performed at the beamline X7B at the National Synchrotron Light Source (NSLS) of Brookhaven National Laboratory (BNL) with a wavelength of 0.9200 Å. XRD patterns were recorded with a MAR345 image plate. The experimental setup for $d$-spacing measurement was calibrated with the National Institute of Standards and Technology (NIST) polycrystalline Si and $LaB_6$ standards. General structural analysis system (GSAS)[14] with the graphic user's interface (EXPGUI)[15] software was used to analyze the XRD results.

Transmission electron microscopy (TEM) samples were prepared by ultrasonicating the annealed powder in acetone for about half an hour and dropping the different suspensions onto carbon thin-films supported on copper grids (Ted Pella carbon type-A). The Philips EM 430 (Eindhoven, The Netherlands) and JEOL JEM 3000F (Tokyo, Japan) transmission electron microscopes were used to study the size and size distributions of $Ce_{0.8}Zr_{0.2}O_{2-y}$ samples annealed at different chosen temperatures.

Raman scattering was performed in a backscattering configuration using the 488 nm line of a continuous wave argon ion laser (Coherent Innova 100, Santa Clara, CA) at room temperature. The beam was focused to a spot size of ~2 μm and all incident power was less than 1 mW, to eliminate heating in the samples. A triple spectrometer (SPEX 1877, Edison, NJ, Triplemate with 0.6 m) in subtractive configuration was used to analyze the spectra, and a silicon CCD array detector (SPEX Spectrum One) was used to collect the spectra. Plasma lines were used to calibrate the 80 to 1200 $cm^{-1}$ frequency range (resolution ~2 $cm^{-1}$). All peak intensities and positions were obtained with Lorentzian fitting.

## III. Results

### *(1) TEM*

A high-resolution TEM image of $Ce_{0.8}Zr_{0.2}O_{2-y}$ nanoparticles annealed at 900°C is shown in Fig. 3. The particles are single-crystal grains and exhibit high crystallinity, indicating a solid

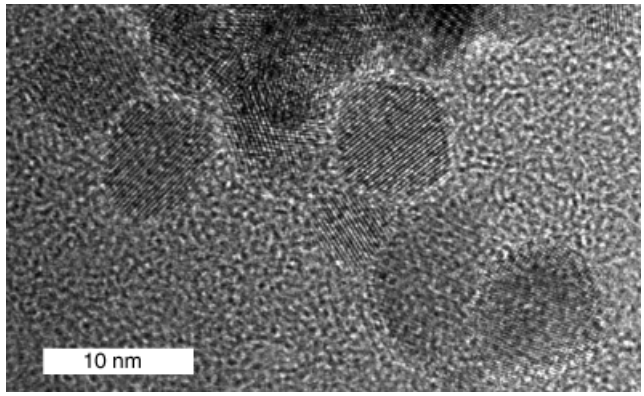


**Fig. 3.** Transmission electron microscopy lattice image of $Ce_{0.8}Zr_{0.2}O_{2-y}$ nanoparticles annealed previously at 900°C.

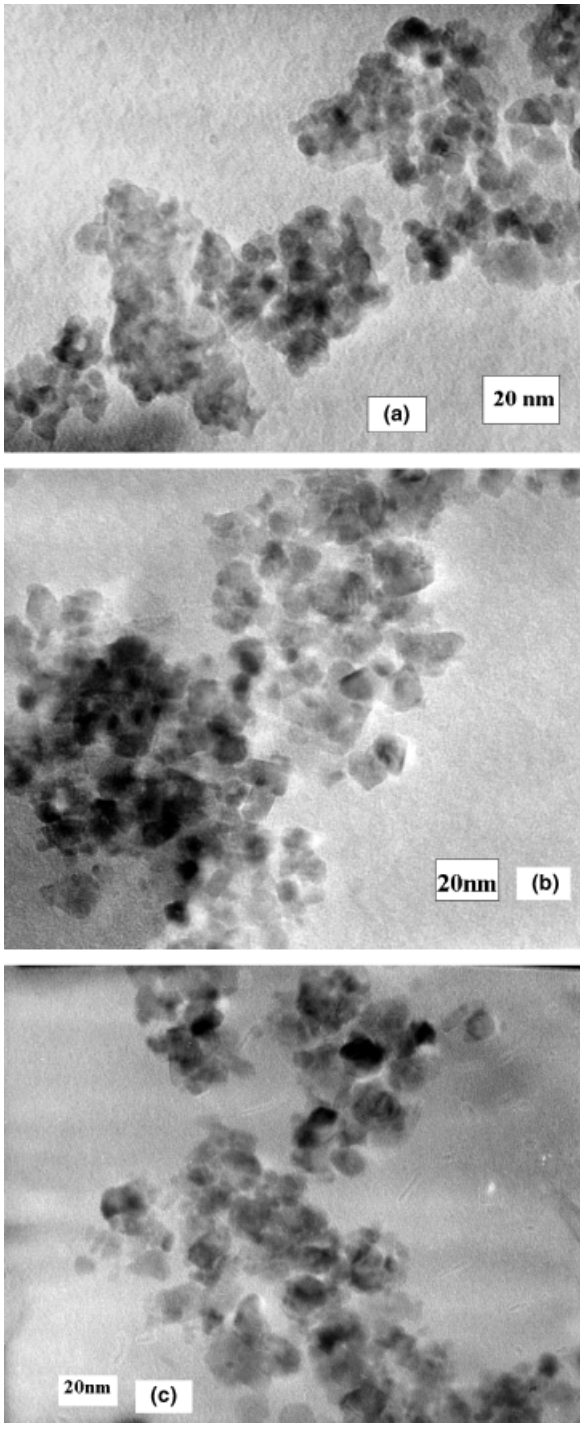


**Fig. 4.** Transmission electron microscopy micrographs of $Ce_{0.8}Zr_{0.2}O_{2-y}$ nanoparticles annealed at various temperatures: (a) 600°C, (b) 900°C, and (c) 1100°C.

solution has been formed. There are few extended defects such as dislocations, grain boundaries, and staking faults observed inside particles. Three TEM micrographs (Figs. 4(a)–(c)) show nanoparticles after annealing at 600°, 900°, and 1100°C. It is evident that a higher annealing temperature results in a larger particle size. At least 50 particles were examined from each sample to provide results on particle size and size distribution (see Table I). With increasing annealing temperature, both the particle size and size dispersion increase.

### *(2) XRD*

Rietveld analysis utilizes the whole XRD spectra to determine the long-range structure of crystalline materials. The method is particularly useful in determining the amounts of each phase (phase percentages) for samples with mixed phases. A fitted XRD pattern of $0.1CeO_2$–$0.9ZrO_2$ nanoparticles annealed in air at 1200°C shows a mixture of 8% cubic ($c'$) and 92% tetragonal ($t$) phases (Fig. 5). This method is used to determine the lattice parameters, phase percentages, and crystal sizes of $c'$ phase in nanoparticle samples. All crystal sizes of the $c'$ phase for different annealing temperatures of $(1-x)CeO_2$–$xZrO_2$ are listed in Table II. Crystallite sizes versus composition series are measured for different annealing temperatures. Note the XRD sizes are in agreement with those from TEM analysis. From Table II, there are two noticeable trends. First, the $c'$ crystal size increases from 16 to 81 nm with an increase annealing temperature from 800° to 1250°C. This increase is faster at the high-temperature range. Second, the crystal size of the $c'$ phase decreases with increasing zirconia content until the $t$ phase starts to form. For the 800°C samples, the crystal size decreases from 16 to 5.4 nm as zirconia increases from 10% to 50%, while for the 1200°C samples the crystal size decreases from 62 to 21 nm as zirconia increases from 10% to 40% and then the $c'$ crystallite size increases with further increase of zirconia as the amount of the $t$ phase increases.

The XRD patterns of $(1-x)CeO_2$–$xZrO_2$ samples annealed at 1200° and 800°C are shown in Figs. 6 (a) and (b), respectively. For the 1200°C series, samples with zirconia concentration up to 40% show a single cubic $c'$ XRD pattern, while the remaining samples with 50% and higher concentration show a mixture of cubic $c'$ and tetragonal $t$ phases. In this series, the $t$ phase first appears in the 50% zirconia sample which has a minimum $c'$ crystal size of 24 nm in the series. The Bragg peaks of the tetragonal $t$ phase become stronger as the zirconia concentration increases from 50% to 90% with the concomitant decrease of the peak intensities of the cubic phase $c'$. In Fig. 7, a magnified view of Fig. 6(a), the cubic Bragg peaks are at their maximum angle at 40% $ZrO_2$ just before the appearance of the tetragonal phase ($t$) at 50% $ZrO_2$ concentration. As the zirconia concen-

**Table I. The Particle Size and Size Distribution (Full-Width at Half-Maximum) of $Ce_{0.8}Zr_{0.2}O_{2-y}$ Nanoparticles Annealed at Different Temperatures from Transmission Electron Micrographs**

| Annealing temperature (°C) | Particle size (nm) | Size distribution (nm) | Size distribution/ particle size (%) |
|---|---|---|---|
| 600 | 6.45 | 2.01 | 31.2 |
| 900 | 9.18 | 2.66 | 29.0 |
| 1100 | 11.1 | 3.83 | 34.4 |

The particle size and size distribution increase with increasing annealing temperature. The size distributions as a percentage of particle size are within ±35% as listed in the last column.

**Table II. Crystal Sizes for Different Annealing Temperatures for the $c'$ Phase from XRD Data**

| | Crystal size (nm) | | | | | |
|---|---|---|---|---|---|---|
| $x$ in $(1-x)CeO_2$–$xZrO_2$ | 1250°C | 1200°C | 1100°C | 1000°C | 900°C | 800°C |
| 0.1 | 81.3 | 61.6 | 45.6 | 27.3 | | 15.7 |
| 0.2 | | 55.3 | (11.1) | | (9.2) | 7.2 |
| 0.3 | | 53.4 | | 16.9 | | 7.4 |
| 0.4 | | 20.6 | | 12.0 | | 6.0 |
| 0.5 | | 24.3 | | 9.8 | | 5.4 |
| 0.6 | | 29.6 | | | | 6.3 |
| 0.7 | | | | | | 6.1 |
| 0.8 | | 32.1 | | | | |
| 0.9 | | 33.4 | | | | 12.9 |

TEM results are in parentheses. The smallest size of a temperature series is underlined. XRD, X-ray analysis; TEM, transmission electron microscopy.

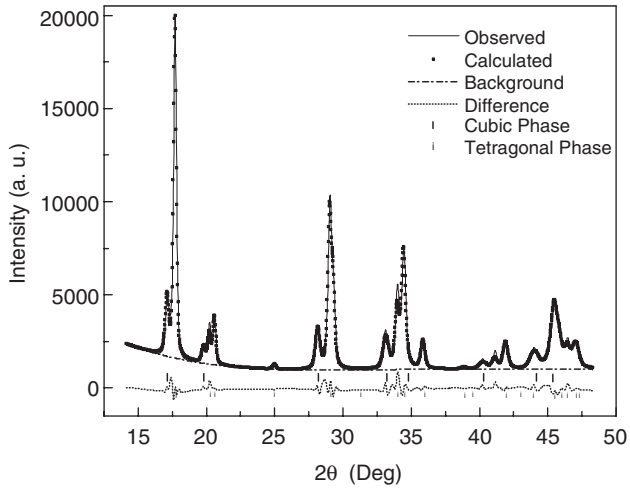


**Fig. 5.** Rietveld analysis of the X-ray diffraction pattern of $0.1CeO_2$–$0.9ZrO_2$ nanoparticles previously annealed at 1200°C.

tration increases from 10% to 40%, the 2θ angle of the (311) peak of the $c'$ phase increases, indicating a lattice contraction with increasing zirconia. Then after the formation of the tetragonal phase ($t$), as shown from the 50% XRD spectrum

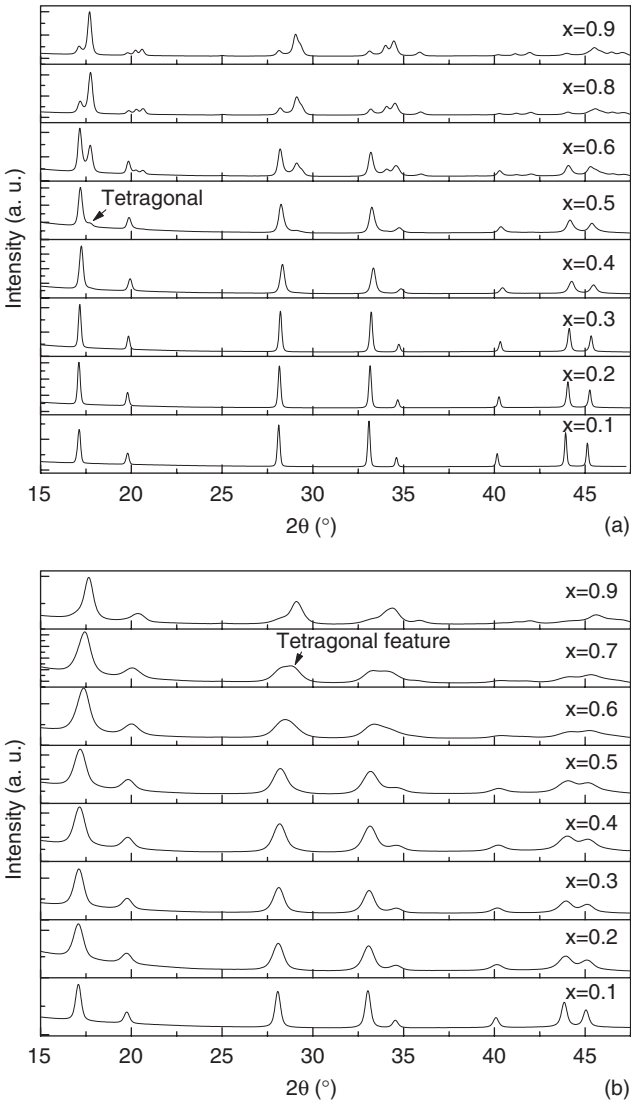


**Fig. 6.** X-ray diffraction patterns of $(1-x)CeO_2$–$xZrO_2$ nanoparticles annealed at (a) 1200°C and (b) 800°C.

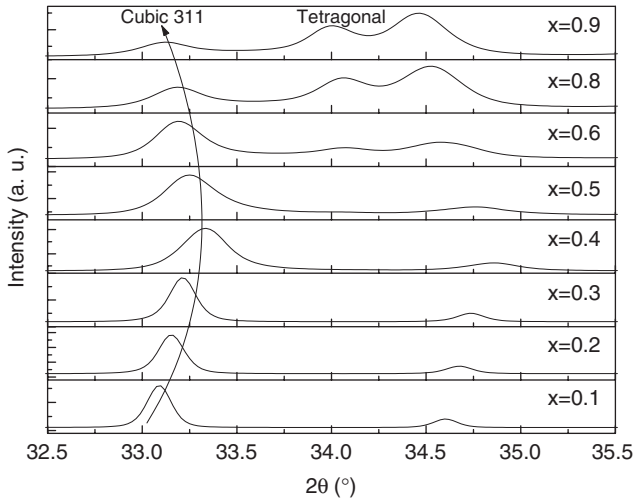


**Fig. 7.** Details of Fig. 6(a).

(see Fig. 6(a)), the (311) peak shifts back to smaller 2θ angles (see Fig. 7), indicating a lattice expansion of the diminishing $c'$ phase. This lattice expansion of the $c'$ phase is likely caused by the segregation of smaller $Zr^{4+}$ ions to the tetragonal $t$ phase leaving the larger $Ce^{4+}$ ions behind. It is, therefore, not accidental that the minimum crystal size coincides with the maximum zirconia content in the $c'$ phase at 40% overall zirconia. The scenario is similar for the 800°C series, but the $t$ phase appears at a higher zirconia concentration of 60% following the minimum crystal size of 5 nm at 50% zirconia (compared with 40% of the 1200°C series).

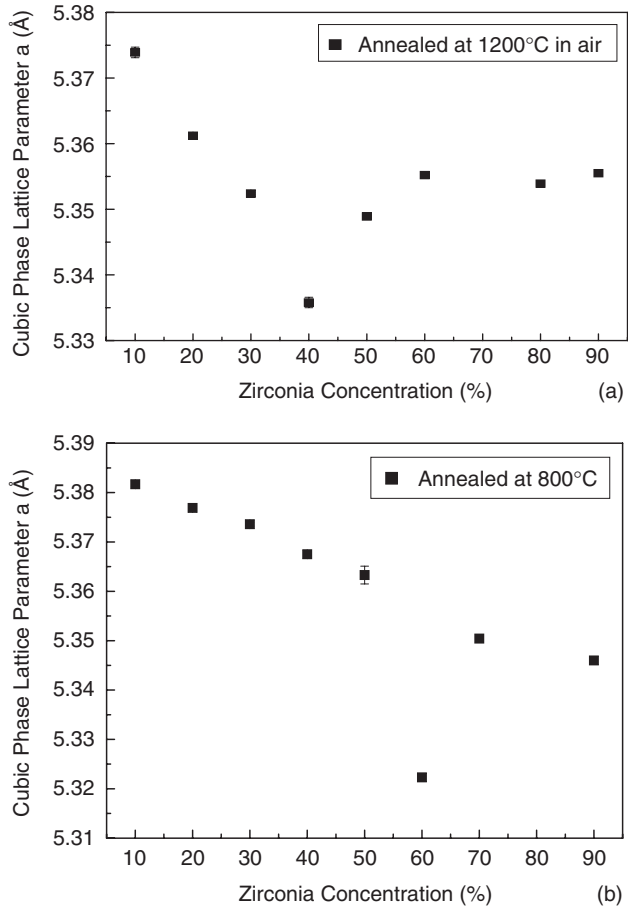


**Fig. 8.** The lattice parameters of the cubic phase $c'$ in $(1-x)CeO_2$–$xZrO_2$. (a) annealed at 1200°C, (b) annealed at 800°C.

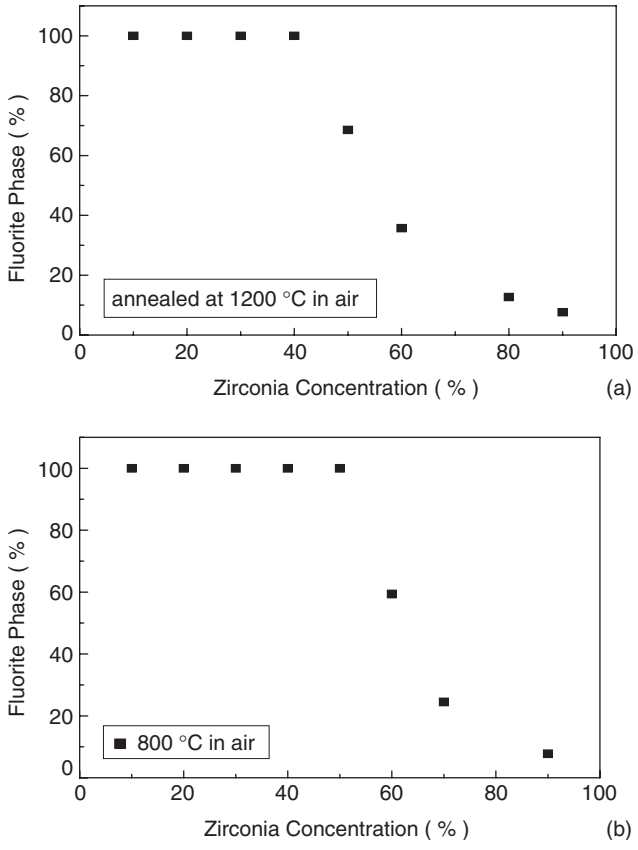


**Fig. 9.** Percentage of cubic phase $c'$ in $(1-x)CeO_2$–$xZrO_2$ annealed in air. (a) annealed at 1200°C, (b) annealed at 800°C.

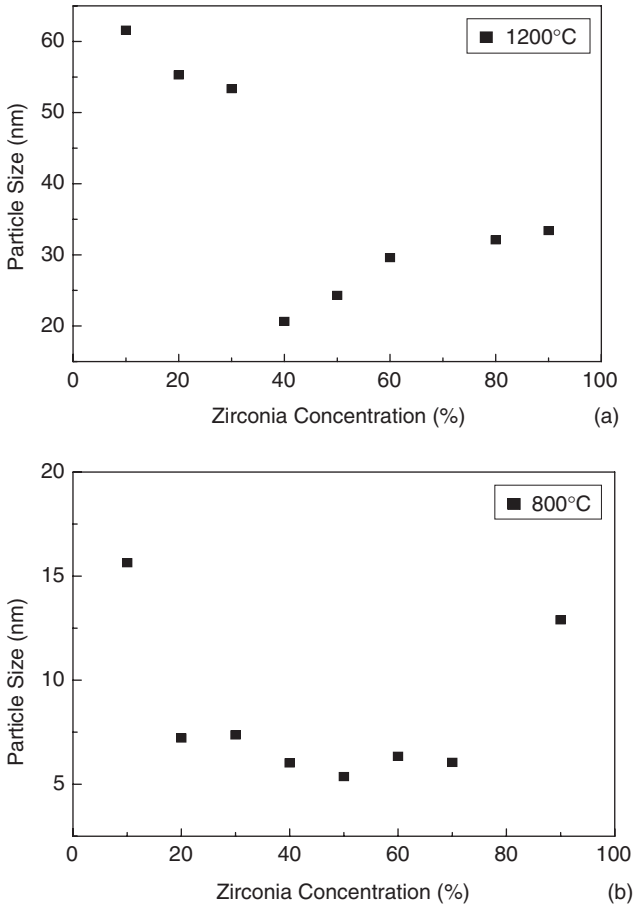


**Fig. 10.** Crystal-size of cubic phase $c'$ $(1-x)CeO_2$–$xZrO_2$ from X-ray diffraction data annealed in air at (a) 1200°C, and (b) 800°C.

From the XRD spectra, the lattice parameter, phase percentage, and crystal size of the cubic phase $c'$ are obtained and presented in Figs. 8–10 and Table II, as a function of zirconia concentration. For the 1200°C samples, the lattice parameter of the $c'$ phase decreases with increasing zirconia concentration and reaches a minimum for $Ce_{0.6}Zr_{0.4}O_{2-y}$ (Fig. 8(a)). This is reasonable as zirconium has a smaller tetravalent cation than cerium. Above 40% zirconia concentration, the lattice parameter of the $c'$ phase increases, while the $c'$ phase percentage diminishes (Fig. 9(a)). This suggests that the zirconia segregates to the tetragonal $t$ phase as soon as this phase emerges between 40% and 50% zirconia. This segregation increases with the zirconia content to 90% with increasingly less zirconia left in the $c'$ phase, while there is a notable increase of $c'$ crystal size (Table II) and its lattice parameter (Fig. 8). The amount of the tetragonal $t$ phase (i.e., 1-[$c'$ phase fraction]) increases with increasing overall zirconia concentration from 50% to 100% (Fig. 9(a)). Similar results correlating the $c'$ phase crystal size, lattice parameter, and the growth of the tetragonal phase $t$ are found in the samples annealed at 800°C, but the emergence of the tetragonal phase, the minimum lattice parameter, and minimum crystal size for the $c'$ phase appear at the higher zirconia contents of 60%, 60%, and 50%, respectively versus 50%, 40%, and 40% for the 1200°C series (see Figs. 8–10 and Table II).

Stability of nanoparticle size against coarsening is important for catalytic activities.[5] Such coarsening is thermally activated and faster at higher temperatures. For samples of 10% zirconia annealed between 800° and 1250°C, the particle size of the $c'$ phase progressively increases from 16 to 81 nm (see Table II). A significant difference in crystal sizes is found in the two series of samples annealed at two different temperatures, 800° and 1200°C. The nanoparticles annealed at 800°C (6–16 nm) are three to four times smaller than those annealed at 1200°C (21–62 nm). The size of the nanoparticles is also a function of the zirconia concentration. For instance, the size ranges from 20 to 33 nm for zirconia concentration from 40% to 90%, while the size is larger from 62 to 54 nm with lower zirconia concentrations (i.e., 10%–30%) at 1200°C. For the two series of samples, the smallest crystal sizes are obtained at 40% zirconia concentration for the 1200°C samples and 50% for the 800°C samples, indicating the best thermal stability against coarsening is located around the 40%–50% zirconia composition.

Unlike previous results,[9,10,16] no $t'$ phase is observed in this study. This is reasonable, as the $t'$ phase, a known metastable phase, originates from a diffusionless phase transformation from $t''$.[17] Diffusionless phase transformation, also known as martensitic transformation, usually requires large undercooling and extra driving forces to occur, particularly when new interfaces and shape changes are required. In most cases, high-stress concentration at extended defects such as dislocations help to initiate martensite formation. In Yashima *et al.*,[9] the $(1-x)CeO_2$–$xZrO_2$ samples were first prepared at 1600°–1760°C in a reducing environment. Then the oxygen was restored by

**Table III. Raman Peak Position ($cm^{-1}$) of the Tetragonal Mode 4/Cubic Peak at Room Temperature, for Compositions and Annealing Temperatures Shown**

| $x$ in $(1-x)CeO_2$–$xZrO_2$ | 1250°C | 1200°C | 1100°C | 1000°C | 800°C |
|---|---|---|---|---|---|
| 0.1 | 474.5 | | 471.1 | 470.5 | 468.8 |
| 0.2 | | 482.6 | | | 467.5 |
| 0.3 | | 479.0 | | 474.0 | 469.5 |
| 0.4 | | 480.0 | | 476.8 | 468.9 |
| 0.5 | | 478.7 | | 479.1 | 469.3 |
| 0.6 | | 475.6 | | | 469.6 |
| 0.7 | | | | | 469.3 |
| 0.8 | | 472.6 | | | |
| 0.9 | | 471.7 | | | 464.1 |

annealing the samples in oxygen at 620°C for 1 h. Hence, high stress from the local volume change during oxidation was expected. In Trovarelli *et al.*,[10] the samples were prepared by high-energy mechanical milling. In both cases, where the $t'$ phase was observed, the final $(1-x)CeO_2$–$xZrO_2$ products were highly strained materials. Our preparation, a solution method and subsequent high-temperature anneal for homogeneity, yields nanocrystals with little aggregation and few extended defects as shown in the TEM results (Figs. 3 and 4). Compared with previous studies, the strain energy is considerably low in our materials. This may explain why the $t'$ phase was not observed in this study. In Yashima *et al.*,[9,16] no pseudo-cubic phase $c'$ was observed at high zirconia concentration. But, in this study the $c'$ phase co-exists with the $t$ phase even at zirconia concentration as high as 90%. This extended composition stability of the $c'$ phase is significant for applications that require mobile oxygen ions.[1–3] Significant redistributions of zirconium ions between the $c'$ and the $t$ phases were observed, which is consistent with the fact that the $t$ phase formation involves zirconium diffusion. Therefore, the tetragonal phase $t$ is a stable phase in the ceria–zirconia ($CeO_2$–$ZrO_2$) binary oxide system for the correct composition and particle-size ranges.

The applicability of earlier $CeO_2$–$ZrO_2$ phase diagrams[8,9] to predict phases observed in nanoparticles in the intermediate composition region proves inadequate. Various preparations,[8–10,16] including ours, have resulted in different observed phases. When particle size approaches the nanoscale, the phase stability becomes significantly affected. For instance, when particles are in the micrometer range, the corresponding $c'$–$t'$ phase boundary is at 33% zirconia concentration. Here, when the particle size is around 20 nm, the $c'$–$t$ phase separation occurs at 40%–50% zirconia concentration and the $t'$ phase is not observed. When the particle size decreases to 6 nm, the $c'$–$t$ phase separation boundary increases to 50%–60% of zirconia concentration and the $t'$ phase is not observed.

### *(3) Raman Scattering*

Although Raman scattering alone is limited in its ability to identify different phases, its use with XRD provides invaluable information. Here, for example, Raman scattering can differentiate the $t''$ and $c$ phases within $c'$, the fluorite

*$Ce_{1-x}Zr_xO_2$ solid solution*: When the crystal symmetry is lower, more Raman modes are usually allowed. The Raman spectra

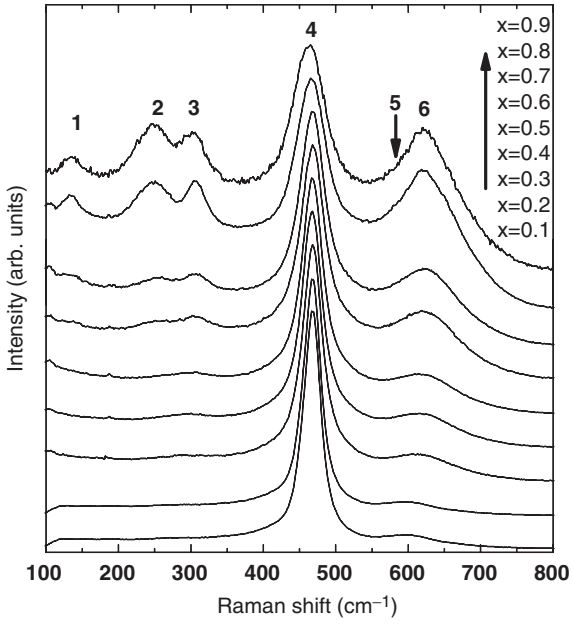


**Fig. 11.** Raman spectra of $(1-x)CeO_2$–$xZrO_2$ samples annealed at 800°C.

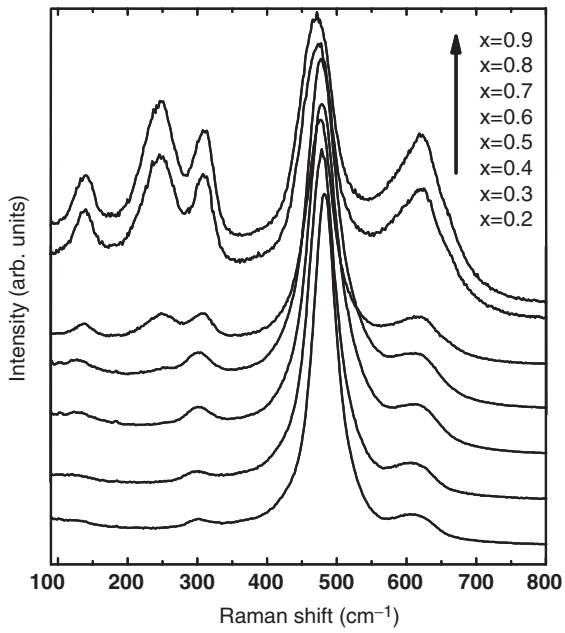


**Fig. 12.** Raman spectra of $(1-x)CeO_2$–$xZrO_2$ samples annealed at 1200°C.

of $(1-x)CeO_2$–$xZrO_2$ nanoparticles annealed at 800° and 1200°C are shown in Figs. 11 and 12, respectively.

For a high zirconia concentration of 90% which has 92% $t$ phase for 800°C annealing, six distinct Raman peaks appear at 131, 247, 307, 464, 596, and 626 $cm^{-1}$ (see spectrum $x = 0.9$ in Fig. 11). These peaks are designated as peaks 1–6 for all samples, even though the exact peak positions vary with zirconia content and particle size (different annealing temperature). Peaks 5 and 6 often overlap, while peak 4 of the tetragonal overlaps with the strong cubic Raman peak at 464 $cm^{-1}$. Peak 4 of the tetragonal phase is weaker than peak 3 near 307 $cm^{-1}$. Therefore, a strong 464 $cm^{-1}$ peak with a weak 307 $cm^{-1}$ peak indicates the presence of the cubic $c$ phase, which is present in every sample except pure $ZrO_2$. For the 800°C sample series, the two lowest frequency peaks (131 and 247 $cm^{-1}$) disappear when the zirconia concentration decreases to 50% zirconia, while peak 3 remains evident until the zirconia concentration decreases to below 30%. Peak 3 is still evident at 20% zirconia for the 1200°C sample series.

Table III gives the Raman shifts for these overlapping tetragonal mode 4/cubic mode peaks, while Table IV gives the Raman shifts for tetragonal peak 3. The Raman mode frequencies vary with zirconium content (Tables III and IV). The Raman band in the 600 $cm^{-1}$ range in ceria has been attributed to defects[18,19] and oxygen displacements that distort the cubic structure, breaking the cubic symmetry and selection rules of the cubic space group[20]. Raman spectra of tetragonal $ZrO_2$ ($t$) show this peak having the highest frequency centered at about 650 $cm^{-1}$ accompanied by a low-frequency shoulder, centered around 620 $cm^{-1}$.[21] The appearance of this band for low zirconia concentration samples, its intensity increase with higher zirconia concentration, and its large width skewing towards

**Table IV. Raman Peak Position ($cm^{-1}$) of the Tetragonal Mode 3 at Room Temperature, for Compositions and Annealing Temperatures Shown**

| $x$ in $(1-x)CeO_2$–$xZrO_2$ | 1200°C | 1000°C | 800°C |
|---|---|---|---|
| 0.3 | 299.9 | 304.4 | 299.5 |
| 0.4 | 300.9 | 302.9 | 295.7 |
| 0.5 | 302.2 | 307.9 | 303.2 |
| 0.6 | 305.7 | | 309.0 |
| 0.9 | 310.2 | | 306.7 |

650 $cm^{-1}$ with increasing zirconia content suggest that this band is associated with $t$ phase-like lattice distortions and their associated defects. The shift to this band to higher frequency is associated Zr ions in ceria and accompanied by lattice distortion. The 307 $cm^{-1}$ Raman peak helps determine the lowest zirconia concentration when the $t''$ phase appears in addition to the $c$ phase. The $t''$ phase appears as $x$ increases to 0.4 and 0.5 for the $c'$ crystallite annealed at both 1200°C (24 nm) and 800°C (5 nm), respectively. The $c'$ phase is persistent, even at $x = 0.9$ there is 8% $c'$ phase from Rietveld analysis for both 33 nm (1200°C) and 13 nm (800°C) samples. Between 90% and 100% zirconia content, the $c'$ phase disappears and only $t$ remains.

The Raman shifts in Table III of the tetragonal mode 4/the cubic mode are indicative of the mode for the cubic phase of the solid solution nanoparticle for all zirconia fractions except for pure zirconia, because the cubic peak is dominant. For a given particle set, i.e., annealing temperature, there is no large variation of shift with $x$ within this range. Within experimental uncertainty, there is a monotonic decrease of this shift with smaller particle size for each $x$. In Spanier *et al.*,[18] the authors attributed such a trend in ceria nanoparticles to successively more phonon confinement and lattice expansion with successively smaller particles. These two contributions are likely important in these solid solution nanocrystals.

A semiquantitative assessment of the relative abundance of each phase, $f_t$, $f_{t''}$, and $f_c$, with $f_t+f_{t''}+f_c = 1$ (and $f_{t'} = 0$), is made using the XRD data and the relative intensities of the Raman peaks 3 and 4, $I_3$ and $I_4$, in Table V. The XRD data give the fraction of $t$ ($f_t$) and $t''/c$ ($f_{t''}+f_c = f_{c'} = 1–f_t$) phases. Absent experiment or theoretical measures for calibration, it is assumed that the Raman spectra of the $t$ and $t''$ phases are the same and that the Raman spectra for these tetragonal phases are the same for each composition, with the six tetragonal peaks having the same absolute peak intensities for the same amount of material probed. The intensities of peaks 3 and 4 can then be expressed as

$$I_3 = \alpha(f_t + f_{t''}) \quad (1)$$

and

$$I_4 = \beta(f_t + f_{t''}) + \gamma f_c \quad (2)$$

and Eq. (2) includes the overlap of the tetragonal peak and the cubic phase. Dividing these two equations gives

$$I_3/I_4 = 1/\{(\beta/\alpha) + (\gamma/\alpha)[f_c/(f_t + f_{t''})]\} \quad (3)$$

Peak 4 is always stronger than peak 3 here, even though it is weaker in tetragonal material. From the Raman spectra of tetragonal zirconia, $\beta/\alpha = 0.86$. Using this approach, Eq. (3) gives roughly consistent results for the data with $\gamma/\alpha = 18–30$ for $x = 0.5–0.6$ and usually consistent results for $\gamma/\alpha$ nearer 30 for smaller $x$ (Table V). These results should be viewed as semiquantitative with $f_i$ accurate to $\pm \sim 0.1$. This analysis confirms that in all of the nanoparticle ensembles studied, peak 4 is mostly because of scattering from cubic material, even when most of the material is tetragonal.

Table V shows that for the 800°C series, the fraction of $t''$ phase is ~33% (5.4 nm) and ~23% (6.3 nm), in 50% and 60% zirconia samples, respectively. Similarly, for the 1200°C series, the $t''$ phase is present at $x = 0.5$ (24 nm), 0.6 (30 nm), 0.8 (32 nm) and 0.9 (33 nm) with the phase percent of ~29%, 7%, 5%, and 2%, respectively. Below 30% $ZrO_2$, only the broad band around 600 $cm^{-1}$ and the strong cubic 464 $cm^{-1}$ peak remain. There is XRD evidence of the absence of a $t$ phase at/below 50% (5.4 nm) and 40% (21 nm) zirconia contents.

This analysis assumes that peak 3 is not associated with defects. Weak peaks in ceria nanoparticles near the locations of tetragonal peaks 2 and 5/6 have been seen and have been linked to either defects[22–24]or tetragonal distortions that break the cubic symmetry[18,19]; such additional peaks have not been seen near tetragonal peak 3. No weak peak in ceria particles is seen here near the tetragonal peak 3 shift. Moreover, it is seen here that peak 3 is the same when (reducing) forming gas or (oxidizing) air is flowed through the 5.4 nm diameter, $x = 0.5$ particles at high temperature (450°C). Such treatments increase and decrease oxygen vacancies, respectively, as is evident from the observed color changes. As such, peak 3 in the solid solution nanoparticles is attributed to tetragonal distortion and not to defects.

## IV. Discussion

Tetragonality occurs when the cubic fluorite lattice of ceria becomes critically strained with an increasing concentration of the smaller Zr cations. Three tetragonal phases have been identified in the literature and they are labeled as $t$, $t'$, and $t''$. The $t$ phase forms from a diffusional transformation and is most stable once formed. The $t'$ and $t''$ phases originate from diffusionless transformations and are metastable. The $t''$ phase forms from the $c$ phase and differs from the $c$ phase only in that some oxygen ions are displaced from their ideal fluorite positions to new tetragonal positions, while all cations remain in their fcc positions with a lattice parameter ratio ($c/a$) equal to unity. Together with the fact that Ce and Zr ions are much stronger X-ray scattering centers than oxygen ions, in XRD the $c$ and $t''$ are virtually indistinguishable. However, the two phases have distinctly

**Table V. The Phase Fractions $f_{c'}$ and $f_t$ by XRD and $f_c$ and $f_{t''}$ by Raman Analysis Using the Ratios of the Intensities of the Raman Peaks $I_3$ and $I_4$ for Different Particle Sizes, Overall Compositions, and Sintering Temperatures**

| | 1200°C | | | | | | 800°C | | | | | |
|---|---|---|---|---|---|---|---|---|---|---|---|---|
| | XRD | | | Raman | | | XRD | | | Raman | | |
| $x$ in $(1-x)CeO_2$-$xZrO_2$ | size (nm) | $f_{c'}$ | $f_t$ | $I_3/I_4$ | $f_{t''}$ | $f_c$ | size(nm) | $f_{c'}$ | $f_t$ | $I_3/I_4$ | $f_{t''}$ | $f_c$ |
| 0 ($CeO_2$) | 100 | 1.0 | 0 | 0 | 0 | 1.0 | 25 | 1.0 | 0 | 0 | 0 | 1.0 |
| 0.1 | 61.6 | 1.0 | 0 | 0 | 0 | 1.0 | 16 | 1.0 | 0 | 0 | 0 | 1.0 |
| 0.2 | 55.3 | 1.0 | 0 | ~0.02 | 0.29[b] | 0.71[b] | 7.2 | 1.0 | 0 | 0 | 0 | 1.0 |
| 0.3 | 53.4 | 1.0 | 0 | 0.02 | 0.32[b] | 0.68[b] | 7.4 | 1.0 | 0 | ~0.01 | 0.17[a] | 0.83[a] |
| 0.4 | 20.6 | 1.0 | 0 | 0.04 | 0.51[b] | 0.49[b] | 6.0 | 1.0 | 0 | ~0.02 | 0.28[a] | 0.72[a] |
| 0.5 | 24.3 | 0.69 | 0.31 | 0.06 | 0.29[b] | 0.40[b] | 5.4 | 1.0 | 0 | 0.02 | 0.33[a] | 0.67[a] |
| 0.6 | 29.6 | 0.36 | 0.64 | 0.10 | 0.07[c] | 0.29[c] | 6.3 | 0.60 | 0.40 | 0.07 | 0.23[a] | 0.37[a] |
| 0.7 | | — | — | — | — | — | 6.1 | 0.24 | 0.76 | 0.08 | ~0 | ~0.24 |
| 0.8 | 32.1 | 0.13 | 0.87 | 0.37 | 0.05[d] | 0.08[d] | | — | — | — | — | — |
| 0.9 | 33.4 | 0.08 | 0.92 | 0.43 | 0.02[d] | 0.06[d] | 13 | 0.08 | 0.92 | 0.31 | ~0 | ~0.10[d] |
| 1.0 ($ZrO_2$) | 10–25 | Tetragonal (530°C) | | | | | | | | | | |

There is much uncertainty in the Raman analysis of the $x = 0.7$ and 0.9 of the 800°C samples. Error ranges for Raman results are labeled by superscripts: $a = \pm 0.06$, $b = \pm 0.07$, $c = \pm 0.05$, and $d = \pm 0.02$, while the error bars for XRD results are shown in Fig. 9. The particles are sintered at 800°C and 1200°C, While for 100% zirconia they are sintered at 530°C. XRD, X-ray diffraction.

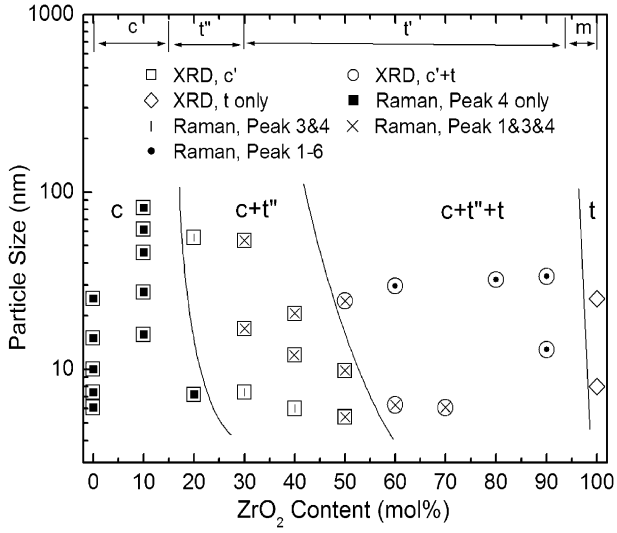


**Fig. 13.** Phase stability diagram of $(1-x)CeO_2$–$xZrO_2$ samples with various crystal size of the $c'$ phase (from Fig. 10 and Table V). There are overlapping symbols to denote X-ray diffraction (XRD) and Raman techniques in phase identification. Open symbols are from the XRD results and the inside symbols are from Raman scattering. Open squares (□), 100% $c'$ phase present from XRD; circles (○), $t$ phase present from XRD; diamonds (◇), only $t$ phase present from XRD. Inner symbols, solid squares (■), only Raman peak 4 is present; vertical line (|); only Raman peaks 3 and 4 are present; crosses (×), only Raman peaks 1, 3 and 4 are present; dots (●), all Raman peaks 1–6 are present. At the top of the diagram are the phase fields identified in Yashima *et al.*[9] from reduced-quench-re-oxidized bulk/micron-size samples.

different Raman spectra. The appearance of peak 3 can be used to mark the onset of tetragonality.[9,25] Samples with zirconia content of 30% annealed at 800°C (7 nm) show this tetragonal mode and this concentration marks the appearance of the $t''$ phase.

The phase diagram published by Yashima shows the $t$ phase as a high-temperature phase[9] (see Fig. 2). The two-phase region below 1200°C between the $c$ and monoclinic $m$ contains two $T$ lines marking diffusionless transformations of $c$ to $t''$ and $t''$ to $t'$ as temperature decreases and zirconia content increases. In the Yashima samples, it is possible to have $c$, $m$, $t''$ and even $t'$ co-exist provided the martensitic transformations are incomplete. Compared with normal diffusion phase transformations, martensitic phase transformations involve a shape change of the unit cell, and require extra driving force to continue the transformation. Therefore, the material involved seldom has a complete transformation. For our samples, the $t$ phase forms from short-range diffusion of Zr ions within the $t''$ phase, a supersaturated fluorite solid solution with zirconia in excess. The short distance for diffusion makes the $t$ phase formation more accessible in nanoparticles than in bulk. The likely scenario is that there is not enough driving force left to nucleate $t'$ phase from $t''$.

Results from XRD and Raman scattering are summarized in Table V and visually displayed in Fig. 13, showing the phases observed at different compositions and different crystal sizes. To estimate the extent the diagram is useful, we need to keep in mind that coarsening by half-an-hour annealing is observed not to happen below 450°C.

As the zirconia content increases, the appearance of the $t$ phase and the disappearance of the $c'$ phase are determined by the XRD data. Conversely, the appearance of the $t''$ phase from the cubic $c$ phase is determined by the appearance of Raman peak 3.

It is clear from XRD results that when the particle size decreases, the boundary between the $c'$ and the $c'+t$ phase regions, as marked by the appearance of the $t$ phase XRD peaks, shifts to a higher zirconia concentration (see Fig. 13). For the pure $ZrO_2$ nanoparticles smaller than 30 nm, the XRD data only show the tetragonal structure and none of the monoclinic peaks. The total disappearance of the $c'$ phase between 90% and 100% $ZrO_2$ establishes a phase boundary between the $c'+t$ and $t$ regions between 90% and 100% $ZrO_2$. The $c'$, the $c'+t$, and the $t$ phase regions can be further broken down with the Raman data into the $c$, the $c+t''$, the $c+t''+t$, and the $t$ regions. The three phase region of $c+t''+t$ does not seem consistent with the phase rule for a binary system, but the present situation can be explained by two factors. First, it is normal to have an incomplete martensitic transformation. Second, there is coherence between the $c$ and $t''$ phases and coherence between phases has resulted in more distinct phases than predicted by the phase rule.[26]

The boundary between the $c'$ and the $c'+t$ phase regions is then really the boundary between the $c+t''$ and the $c+t''+t$ phase regions and is marked by the appearance of the $t$ phase peaks in XRD. The boundary between the $c$ and the $c+t''$ phase regions is marked by the appearance of the $t''$ Raman peaks. The boundary between $t$ and $c+t''+t$ phase regions is marked by the total disappearance of the $c'$ XRD peaks. Similar to the $c'/c'-t$ boundary, the $CeO_2$–$ZrO_2$ t/monoclinic boundary also shifts to a higher zirconia concentration (i.e., 100%) with smaller particles. Consistently, the monoclinic phase is not observed in our nanoparticle samples. Our results agree with earlier results that smaller particle size helps to stabilize the high-temperature tetragonal phase at room temperature over the monoclinic phase.[27,28] In some cases, cubic structure also has been observed in the nanocrystalline $ZrO_2$.[28–31] The stability of the metastable $ZrO_2$ tetragonal phase at room temperature is significantly affected by the particle size, surface energy, strain, as well as grain boundaries.[27,28] Similarly, these influencing factors are likely to affect stability of different phases within the $CeO_2$–$ZrO_2$ binary oxide system.

## V. Conclusions

The occurrence of different phases (cubic $c$, tetragonal $t''$ and $t$) in the $CeO_2$–$ZrO_2$ binary nanoparticle system is studied by synchrotron XRD, TEM, and Raman scattering. Neither the metastable tetragonal $t'$ phase nor the monoclinic $m$ phase is observed. The nanoscale of the particles likely stabilizes the tetragonal $t$ phase against the formation of the monoclinic phase even at 100% zirconia. This is similar to the tetragonal $t$ phase in embedded zirconia in transformation-toughened ceramics. Both the $c-t''$ and the $c'-t$ phase boundaries shift to higher zirconia concentrations as the particle size decreases. The zirconia solubility limit increases with decreasing particle size such that the $c$ and $t''$ phases can be sustained at higher concentrations of zirconia before the corresponding formation of the $t''$ and $t$ phases. Raman scattering and XRD agree with each other in determining the emerging compositions of the $t$ phase in the 1200° and the 800°C samples. The nanoparticles exhibit different phases than those expected from the bulk in the $CeO_2$–$ZrO_2$ binary system. Therefore, nanoparticles of 20 nm and smaller having composition of 35%–40% zirconia in ceria are 100% $c'$ and stable against coarsening. Similar to the $c$ phase, the $t''$ phase likely contributes to OSC.

## Acknowledgments

FZ acknowledges Mr. L. Cranswick (www.ccp14.ac.uk) for teaching various XRD analysis programs and Ms. Millicent Smith (supported by Columbia University Materials Research Science and Engineering Center (MRSEC) Research Experiences for Undergraduates (REU) program) for helping with the initial synthesis of the ceria-zirconia nanoparticles.

## References

[1]A. Trovarelli, C. de Leitenberg, M. Boaro, and G. Dolcetti, "The Utilization of Ceria in Industrial Catalysis," *Catal. Today*, **50** [2] 353 (1999).

[2]B. C. H. Steele and A. Heinzel, "Materials for Fuel-Cell Technologies," *Nature*, **414** [6861] 345 (2001).

[3]Q. Fu, H. Saltsburg, and M. Flytzani-Stephanopoulos, "Active Nonmetallic Au and Pt Species on Ceria-Based Water-Gas Shift Catalysts," *Science*, **301** [5635] 935 (2003).

[4]J. A. Rodrigues, X. Wang, J. C. Hanson, G. Liu, A. Iglesias-Juez, and M. Fermandes-Garcia, "The Behavior of Mixed-Metal Oxides: Structural and Electronic

Properties of $Ce_{1-x}Ca_xO_2$ and $Ce_{1-x}Ca_xO_{2-x}$," *J. Chem. Phys.*, **119** [11] 5659 (2003).

[5]J. A. Rodrigues, J. C. Hanson, J.-Y. Kim, G. Liu, A. Iglesias-Juez, and M. Fermandes-Garcia, "Properties of $CeO_2$ and $Ce_{1-x}$ $Zr_xO_2$ Nanoparticles: X-Ray Absorption Near-Edge Spectroscopy, Density Functional, and Time-Resolved X-Ray Diffraction Studies," *J. Phys. Chem. B*, **107**, 3535 (2003).

[6]S. Bernal, J. J. Calvino, G. A. Cifredo, D. Finol, J. M. Gatica, C. J. Kiely, C. Lopez-Cartes, J. G. Zheng, and H. Vidal, "Study of the Structural Modifications Induced by Reducing Treatments on a $Pd/Ce_{0.8}Tb_{0.2}O_{2-x}/La_2O_3$–$Al_2O_3$ Catalyst by Means of X-Ray Diffraction and Electron Microscopy Techniques," *Chem. Mater.*, **14** [3] 1405 (2002).

[7]T. Miki, T. Ogawa, M. Haneda, N. Kakuta, A. Ueno, S. Tateishi, S. Matsuura, and M. Sato, "Enhanced Oxygen Storage Capacity of Cerium Oxides in $CeO_2$/$La_2O_3$/$Al_2O_3$ Containing Precious Metals," *J. Phys. Chem.*, **94** [16] 6464 (1990).

[8]P. Duwez and F. Odell, "Phase Relationships in the System Zirconia–Ceria," *J. Am. Ceram. Soc.*, **33** [9] 274 (1950).

[9]M. Yashima, H. Arashi, M. Kakihana, and M. Yoshimura, "Raman-Scattering Study of Cubic-Tetragonal Phase-Transition in $Zr_{1-x}Ce_xO_2$ Solid Solution," *J. Am. Ceram. Soc.*, **77** [4] 1067 (1994).

[10]A. Trovarelli, F. Zamar, J. Llorca, C. de Leitenburg, G. Dolcetti, and J. T. Kiss, "Nanophase Fluorite-Structured $CeO_2$–$ZrO_2$ Catalysts Prepared by High-Energy Mechanical Milling – Analysis of Low-Temperature Redox Activity and Oxygen Storage Capacity," *J. Catal.*, **169**, 490 (1997).

[11]F. Zhang, S.-W. Chan, J. E. Spanier, E. Apak, Q. Jin, R. D. Robinson, and I. P. Herman, "Cerium Oxide Nanoparticles: Size-Selective Formation and Structure Analysis," *Appl. Phys. Lett.*, **80** [1] 127 (2002).

[12]F. Zhang, Q. Jin, and S.-W. Chan, "Ceria Nanoparticles: Size, Size Distribution and Shape," *J. Appl. Phys.*, **95**, 4319 (2004).

[13]S.-W. Chan and F. Zhang, US Patent Application PCT/US03/03393.

[14]A. C. Larson and R. B. Von Dreele Los Alamos National Laboratory Report LAUR 86–748. (1994)

[15]B. H. Toby, "EXPGUI, a Graphical User Interface for GSAS," *J. Appl. Cryst.*, **34**, 210 (2001).

[16]M. Yashima, S. Sasaki, Y. Yamaguchi, M. Kakihana, M. Yoshimura, and T. Mori, "Internal Distortion in $ZrO_2$–$CeO_2$ Solid Solutions: Neutron and High-Resolution Synchrotron X-Ray Diffraction Study," *Appl. Phys. Lett.*, **72** [2] 182 (1998).

[17]A. Trovarelli, M. Boaro, E. Rocchini, C. de Leitenburg, and G. Dolcetti, "Some Recent Developments in the Characterization of Ceria-Based Catalysts," *J. Alloys Compd.*, **323–324**, 584 (2001).

[18]J. E. Spanier, R. D. Robinson, F. Zhang, S.-W. Chan, and I. P. Herman, "Size-Dependent Properties of $CeO_{2-y}$ Nanoparticles as Studied by Raman Scattering," *Phys. Rev. B*, **64**, 245407 (2001).

[19]A. Mineshige, T. Taji, Y. Muroi, M. Kobune, S. Fujii, N. Nishi, M. Inaba, and Z. Ogumi, "Oxygen Chemical Potential Variation in Ceria-Based Solid Oxide Fuel Cells Determined by Raman Spectroscopy," *Solid State Ionics*, **135** [1–4] 481 (2000).

[20]P. Fornasiero, G. Balducci, R. DiMonte, J. Kaspar, V. Sergo, G. Gubitosa, A. Ferrero, and M. Graziani, "Modification of the Redox Behaviour of $CeO_2$ Induced by Structural Doping with $ZrO_2$," *J. Catal.*, **164** [1] 173 (1996).

[21]P. Barberis, T Merle-Mejean, and P. Quintard, "On Raman Spectroscopy of Zirconium Oxide Films," *J. Nucl. Mat.*, **246** [2–3] 232 (1997).

[22]J. R. McBride, K. C. Hass, B. D. Poindexter, and W. H. Weber, "Raman and X-Ray Studies of $Ce_{1-x}RE_xO_{2-y}$ , Where RE = La, Pr, Nd, Eu, Gd, and Tb," *J. Appl. Phys.*, **76** [4] 2435 (1994).

[23]W. H. Weber, K. C. Hass, and J. R. McBride, "Raman Study of $CeO_2$: Second-Order Scattering, Lattice Dynamics, and Particle-Size Effects," *Phys. Rev. B*, **48**, 178 (1993).

[24]A. Nakajima, A. Yoshihara, and M. Ishigame, "Defects-Induced Raman Spectra in Doped $CeO_2$," *Phys. Rev. B*, **50**, 13297 (1994).

[25]D. Lamas, G. Lascalea, R. Juarez, E. Djurado, L. Perez, and N. Walsoe de Reca, "Metastable Forms of the Tetragonal Phase in Compositionally Homogeneous, Nanocrystalline Zirconia-Ceria Powders Synthesized by Gel Combustion," *J. Mat. Chem.*, **13** [4] 904 (2003).

[26]J. W. Cahn and F. Larché, "A Simple Model for Coherent Equilibrium," *Acta Metall.*, **32**, 1915–23 (1984).

[27]T. Mitsuhashi, M. Ichihara, and U. Tatsuke, "Characterization and Stabilization of Metastable Tetragonal $ZrO_2$," *J. Am. Ceram. Soc.*, **57** [2] 97 (1974).

[28]R. C. Garvie and M. F. Goss, "Intrinsic Size Dependence of the Phase-Transformation Temperature in Zirconia Microcrystals," *J. Mater. Sci.*, **21**, 1253 (1986).

[29]C. Y. Huang, Z. L. Zhang, Z. T. Zhang, and J. H. Gong, "Study on a New, Environmentally Benign Method and its Feasibility of Preparing Nanometer Zirconia Powder," *Mater. Res. Bull.*, **35** [9] 1503 (2000).

[30]F. Zhang, J. M. Raitano, C.-H. Chen, J. C. Hanson, C. Wolfgang, S. Khalid, and S.-W. Chan, "Cubic Ceria–Zirconia Nanoparticles Stabilized by $Ce^{3+}$ Concentration," *J. Appl. Phys., accepted.*

[31]F. Zhang, P. J. Chupas, S. L. A. Liu, J. C. Hanson, W. A. Caliebe, P. L. Lee, and S.-W. Chan, "*In Situ* Study of the Crystallization Transition from Amorphous to Cubic Zirconium Oxide: Rietveld and Reversed Monte Carlo Analyses," *to be published.* □